Electronic Supplementary Information (ESI)

Chiral Mesostructured $NiFe_2O_4$ Films with Chirality Induced Spin Selectivity

Yiping Zhou,[† a] Te Bai[† b] and Yingying Duan*[a]

[a.] *School of Chemical Science and Engineering, Tongji University, 1239 Siping Road, Shanghai, 200092, P. R. China. E-mail: yyduan@tongji.edu.cn*

[b.] *Wuxi Vocational College of Science and Technology, 8 Xinxi Road, Wuxi, 214028, P.R. China.*

† These authors contributed equally to this work.

Experimental Section

1. Chemicals

$FeCl_3 \cdot 6H_2O$, $Ni(NO_3)_2 \cdot 6H_2O$, urea, L/D-Tyrosine and ethanol were purchased from Sinopharm Chemical Reagent Co., Ltd. The purity of all the reagents are ≥99%, which were used as received without further purification. The deionized (DI) water was obtained from a Milli-Q synthesis system.

2. Substrate activation

The FTO substrates (40×10×1.1 mm, coating thickness = 500 nm, sheet resistance ≤ 15 Ω) were washed with a mixture of acetone and ethanol (V/V = 1:1) and deionized water in an ultrasonic bath for 30 min.

3. Synthesis of CMNFFs

In a typical synthesis, 0.5 mmol tyrosine was dissolved in a mixed solution of 30 mL deionised water and 7 mL ethanol with stirring in a water bath at 50 °C for 1 h. And then, 2.6 mmol $FeCl_3 \cdot 6H_2O$, 1.3 mmol $Ni(NO_3)_2 \cdot 6H_2O$ were added to obtain a homogeneous solution. After the mixture was stirred for 12 h, 10 mmol urea was added with stirring for 15 min. The above mixed solution and cleaned FTO substrate were transferred into a 50 ml Teflon-lined autoclave, and hydrothermally heated at 160 °C for 12 h. After cooling to room temperature, the substrate was washed with DI water and ethanol for several times to remove the unreacted impurities and then dried at 80 °C for 12 h. Finally, CMNFFs were obtained by calcination at 550 °C in air for 6 h.

4. Characterization

Wide XRD patterns were recorded on a Rigaku MiniFlex 600 powder diffractometer equipped with Cu Kα radiation, at the rate of 0.2 $^{o} \cdot min^{-1}$ over the range 20-80°. GI-XRD patterns were recorded on a Rigaku SmartLab 9KW powder diffractometer equipped

with Cu Kα radiation, at the rate of 1 $^{o}\cdot min^{-1}$ over the range 20-80^{o}. SEM images were obtained using JEOL JSM-7100 with accelerating voltage of 5 kV.

The CD spectra were obtained on a JASCO J-1500 spectropolarimeter and data were collected with scanning rate of 500 $nm\cdot min^{-1}$ ranging from 200 to 800 nm at the temperature of 293 K. Current–voltage measurements were performed using Multimode AFM with Nanoscope V controller (Bruker-Dimension icon). I–V spectroscopy measurements were recorded by performing a voltage bias of −3 to +3 V at the tip in a contact mode. For each spectroscopy measurement, the tip was placed in a new position. A magnetic Pt-coated Cr tip (Multi75E-G, BudgetSensors) with nominal spring constant 3 $N\cdot m^{-1}$ was used to acquire I-V curves. The tips are pre-magnetized using a permanent magnet. The hysteresis curves of the samples were measured using a Superconducting Quantum Interference Device (SQUID) based magnetic measurement system (Quantum Design, USA) with magnetic fields in the range of -5-5 T and temperatures of 2-300 K.

Supplementary Figures and Tables

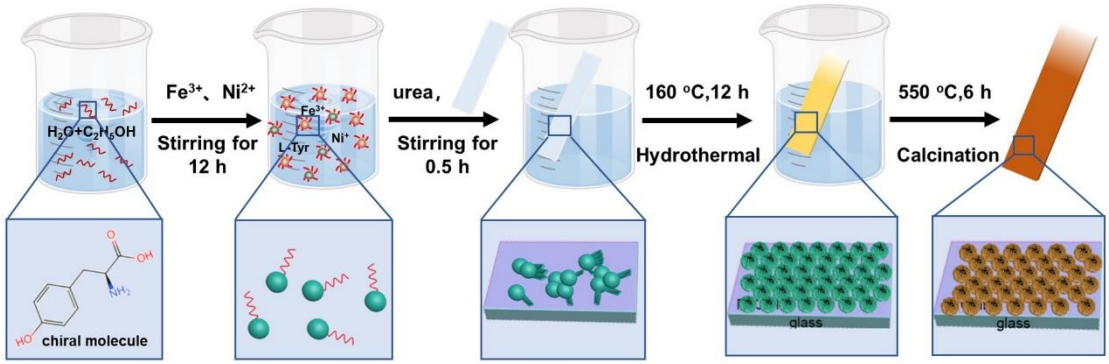

Figure S1. The fabrication strategy for CMNFFs.

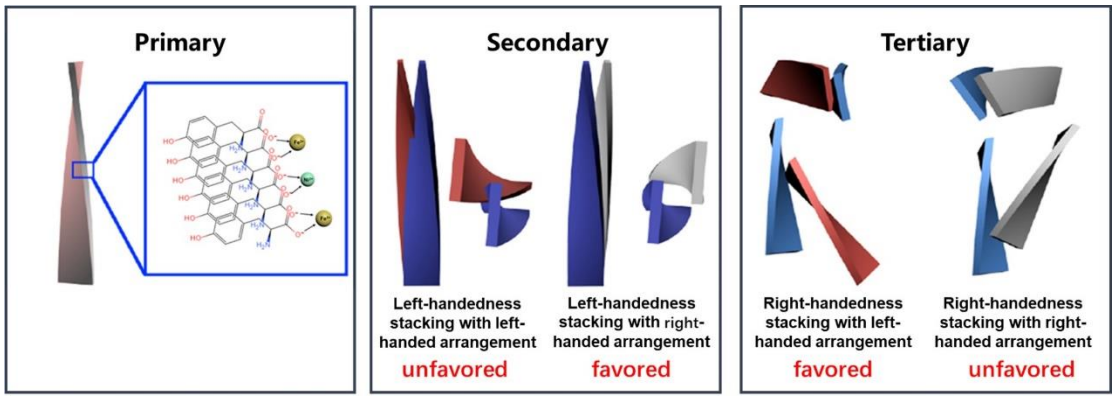

Figure S2. Illustration of chirality transfer from chiral molecules to a L-CMNFF.

The chiral primary structure with left-handed distorted crystal lattice would be induced by the L-Tyr, in which the carboxyl and amino groups chelated well with the Ni^{2+} and Fe^{3+}. After mixing with urea and heating, the Ni^{2+} and Fe^{3+} were deposited to be $NiFe_2O_4$. During the reaction, the chiral arrangement of Tyr molecules would induce the oriented malposed growing of nanocrystals, thus leading to the formation of primary chiral nanoflakes. In another word, the primary chirality of nanoflakes is copied from organic molecules, resulting in the consistence of the primary chirality in the L-CMNFF and the chirality of L-Tyr assemblies showing left-handedness. The secondary chirality is favored to form right-handed arrangement due to the maximum interaction between nanoflakes. Similarly, the tertiary chirality is left-handedness. Consequently, the chirality transfer from the L-Tyr assemblies to left-handed twisted nanoflakes by copying organic structures and then right-handed stacking secondary chirality and left-handed arranged tertiary chirality by self-assembly.

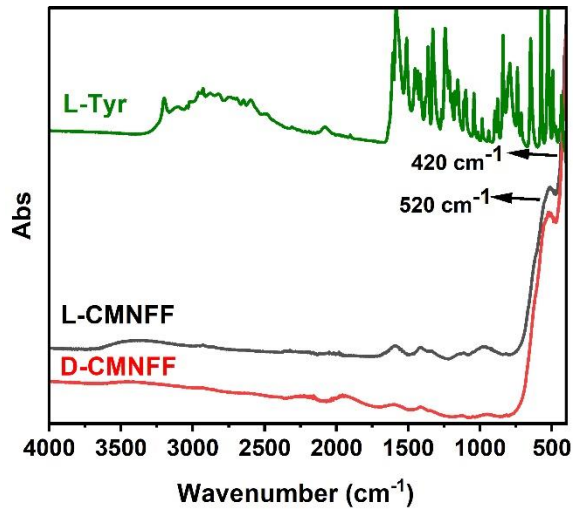

Figure S3. FTIR spectra of antipodal CMNFFs and L-Tyr.

CMNFFs exhibit two absorption bands.The distinct peaks centered at 420 cm^{-1}, 520 cm^{-1} for CMNFFs were associated with metal oxide stretching vibration (Ni-O and Fe-O) in octahedral (B) sites and tetrahedral (A) sites, respectively. The other bands like -COOH, -CO-, -OH peaks are completely vanished after calcination at 550 ºC for 6 h.

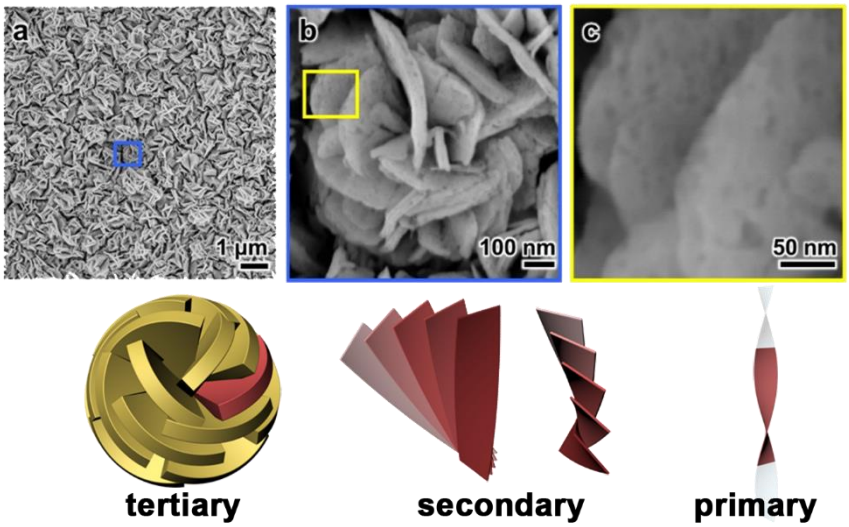

Figure S4. SEM images of an D-CMNFF with varying magnifications, and schematic drawings of the hierarchically chiral structures.

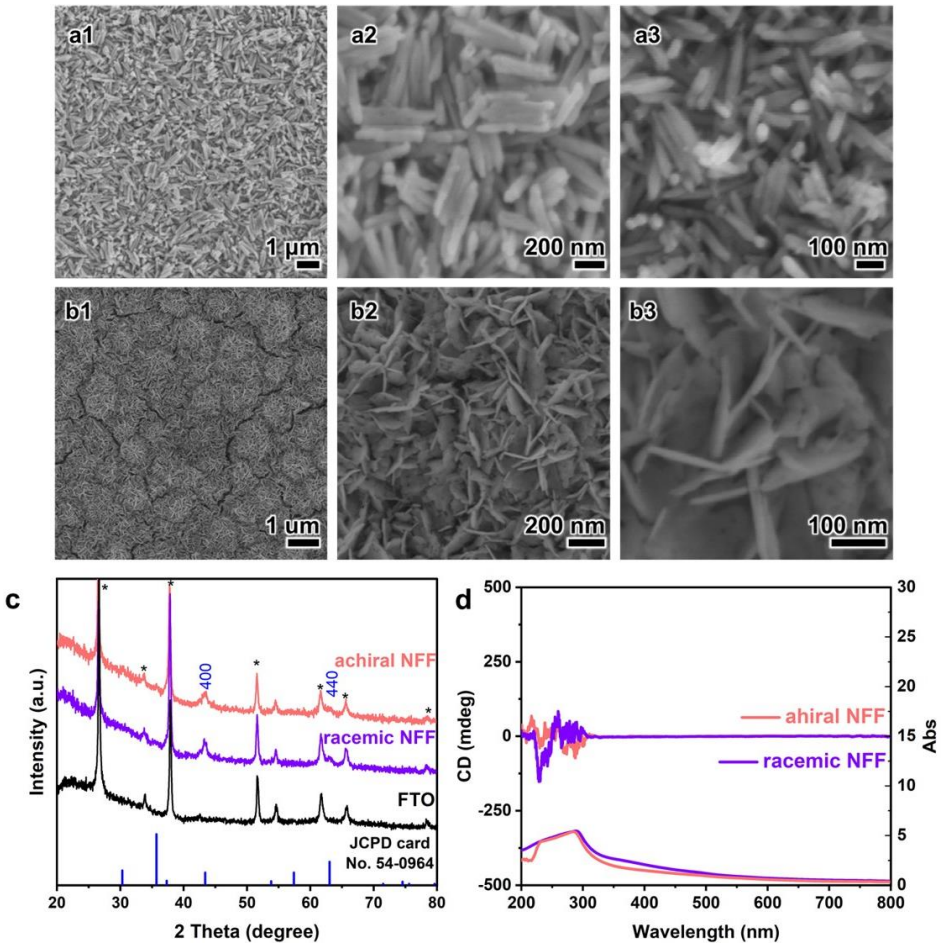

Figure S5. SEM images of achiral NFF (a) and racemic NFF(b) with varying magnifications, wide angle XRD patterns (c), and transmitted CD and UV-Vis spectra (d) of achiral NFF and racemic NFF.

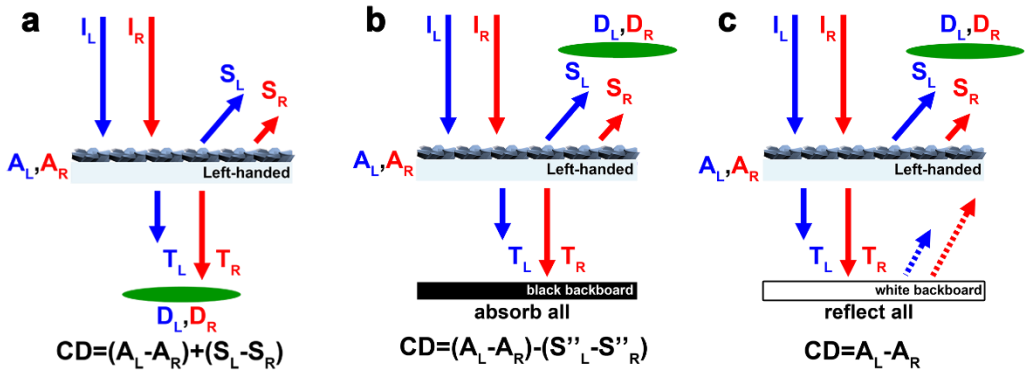

Figure S6. Schematic illustration of CD detection mechanism with a left-handed medium. I, A, T, S, and D are incident, absorbed, transmitted, scattered, and detected circularly polarized light, respectively. The subscripts L and R represent left- and right-handed circularly polarized light.

A medium with a left-handed helical structure preferentially absorbs right-handed circularly polarized (R-CP) light and reflects left-handed circularly polarized (L-CP) light [*Biochemistry* **1988**, 27, 3056-3068]. As shown in the **Figure S6**, there are three different detection modes of our CD spectra measurements:

In the **transmitted CD measurement** (**Figure S6a**):

(i) The incident light from light source is $I_L+I_R(I_L=I_R)$.

(ii) The light partially absorbed by left-handed medium is A_L+A_R ($A_L<A_R$) due to the electron transition from valence band to conductor band.

(iii) At the same time, the light selectively scattered by left-handed structures is S_L+S_R ($S_L>S_R$) due to the circular Bragg resonance, depending on the pitch length of the chiral structures and the optical refractive index of the medium and environments ($\lambda = Pitch \cdot n_{average} \cdot \sin\alpha$, where λ is the wavelength, $Pitch$ is the pitch length, $n_{average}$ is the effective refractive index of the medium and environments, and α is the angle between the incident light and the surface of the chiral film). Therefore, after infiltration with water, the scattering-based OA weakened dramatically because the $n_{average}$ weakened when the interfacial medium changing from $NiFe_2O_4$ (n=2.2)and air (n=1.0) to $NiFe_2O_4$ and water (n=1.3).

(iv) The rest of light transmit (T_L+T_R) and collected by the detector as D_L+D_R.

That is, in the transmitted CD measurement, $D_L=T_L$, $D_R=T_R$.

Therefore, the output signal transmitted $CD=(I_L-D_L)-(I_R-D_R)=(A_L+S_L)-(A_R+S_R)=(A_L-A_R)+(S_L-S_R)$, which includes the absorption-based OA and scattering-based OA. To distinguish these two kinds of OAs, the scattering-based OA can be weakened through changing the environmental medium.

It should be noted that the black and white background are effective only at the visible range, and all scattered light can be collected by an integrating sphere and received by the detector. In the **diffuse-reflection CD with a black background ($DRCD_B$) measurement** (**Figure S6b**):

(i) The incident light from light source is $I_L+I_R(I_L=I_R)$.

(ii) The light partially absorbed by left-handed medium is A_L+A_R ($A_L<A_R$) due to the electron transition from valence band to conductor band.

(iii) At the same time, the light selectively scattered by left-handed structures is S_L+S_R ($S_L>S_R$) due to the circular Bragg resonance, and then collected by the detector is D_L+D_R.

(iv) The rest of light transmit (T_L+T_R) and are absorbed totally by the black backboard.

That is, in the $DRCD_B$ measurement, $D_L=S_L$, $D_R=S_R$.

In this case, there are two conditions: If the resonance wavelengths of absorption and scattering are the same, the $DRCD_B=(I_L-D_L)-(I_R-D_R)=(I_L-S_L)-(I_R-S_R)=(I_L-I_R)-(S_L-S_R)=-(S_L-S_R)$, which exhibits opposite scattered-based OA only; If the resonance wavelengths of absorption and scattering are different, $DRCD_B=(A_L-A_R)_{\lambda1}-(S_L-S_R)_{\lambda2}$.

In the **diffuse-reflection CD with a white background ($DRCD_W$) measurement** (**Figure S6c**):

(i) The incident light from light source is $I_L+I_R(I_L=I_R)$.

(ii) The light partially absorbed by left-handed medium is A_L+A_R ($A_L<A_R$) due to the electron transition from valence band to conductor band.

(iii) At the same time, the light selectively scattered by left-handed structures is S_L+S_R ($S_L>S_R$) due to the circular Bragg resonance, and then collected by the detector.

(iv) The rest of light transmit (T_L+T_R) and are reflected totally by the white backboard, and finally collected by the detector.

That is, in the $DRCD_W$ measurement, $D_L=S_L+T_L$, $D_R=S_R+T_R$.

Therefore, the output $DRCD_W=(I_L-D_L)-(I_R-D_R)=(I_L-S_L-T_L)-(I_R-S_R-T_R)=A_L-A_R$, which is absorption-based OA only.

To distinguish OAs of absorption- and scattering-based OAs, the scattering-based OA signals can be observed in the $DRCD_B$ spectra, while disappeared in the $DRCD_W$ spectra.

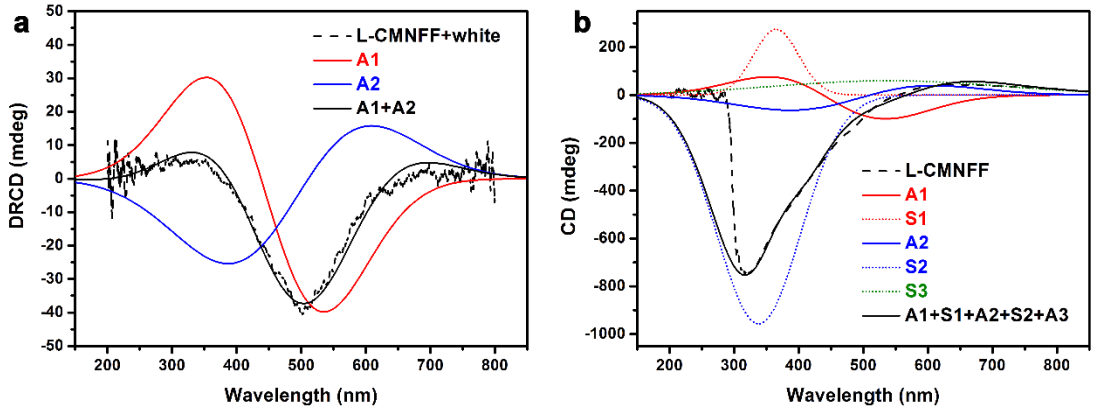

Figure S7. Peak differentiation-simulating analysis of $DRCD_W$ and transmitted CD spectra of L-CMNFF.

There are the multiple OAs of L-CMNFF: (A1) absorption-based OA originates from the primary left-handed twisted nanoflakes; (A2) absorption-based OA originates from the secondary right-handed helical stacking of nanoflakes; (S1) scattering-based OA originates from the primary left-handed twisted nanoflakes; (S2) scattering-based OA arises from secondary right-handed nanoflakes stacking; (S3) scattering OA arises from tertiary micrometer-sized vortexes with left-handed arrangement of nanoplates. The resulting CD signals is the superposed results of these OAs and extinction signals.

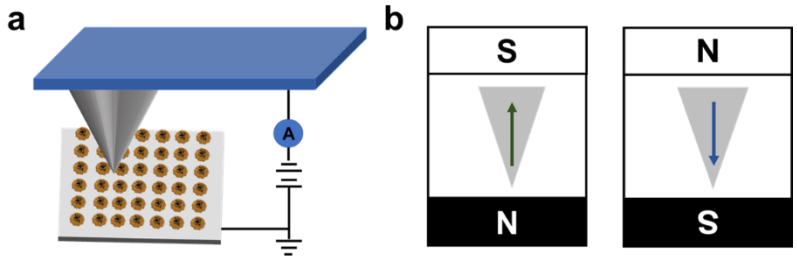

Figure S8. Schematic representation for magnetic-tip conducting atomic force microscopy (mc-AFM).

As shown in **Figure S8**, there is schematic representation for magnetic conducting atomic force microscopy (mc-AFM) measurements. (a) The experimental setup: a magnetic Pt-coated Cr tip (Multi75E-G, BudgetSensors) with nominal spring constant 3 $N \cdot m^{-1}$ was used to acquire I-V curves. The tips are pre-magnetized using a 1.6T permanent magnet. (b) When the tip is pointing to the north pole of the magnet, it is magnetized in the UP direction. (c) When the tip is pointing to the south pole of the magnet, it is magnetized in the DOWN direction.

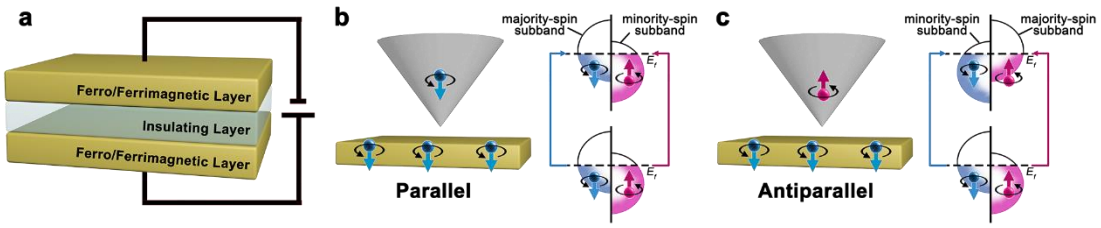

Figure S9. (a) A basic MTJ consists of two ferromagnetic layers separated by a thin insulating layer. (b) Schematic diagram of an MTJ in parallel configuration and its corresponding band diagram, which shows that both spin-up and spin-down electrons can pass through the barrier from the down electrode to the up one. (c) Schematic diagram of an MTJ in antiparallel configuration and its corresponding band diagram. Both spin-up and spin-down channels are blocked due to the asymmetry of two states.

The ferrimagnetism film, the magnetic tip of AFM, and the air between them together form a magnetic tunnel junction (MTJ) as shown in **Figure S9a**. The tunneling conductance or resistance of such a device depends on whether the majority spins of the two electrodes are parallel or antiparallel. It is reported that the origin of tunnel magnetoresistance (TMR) arises from different density of states (DOS) for spin-up and spin-down electrons. Because electron spins are preserved during the transport, each type of spin can only tunnel into the subband of the same spin. Therefore, there will be a high tunneling current (or low resistance) if the majority spins of two electrodes align parallel (**Figure S9b**), which makes the two electrodes have symmetric spin density of states. Otherwise, the antiparallel alignment of the majority spins of two electrodes will generate asymmetric DOS (**Figure S9c**), resulting in low tunneling current (or high resistance).

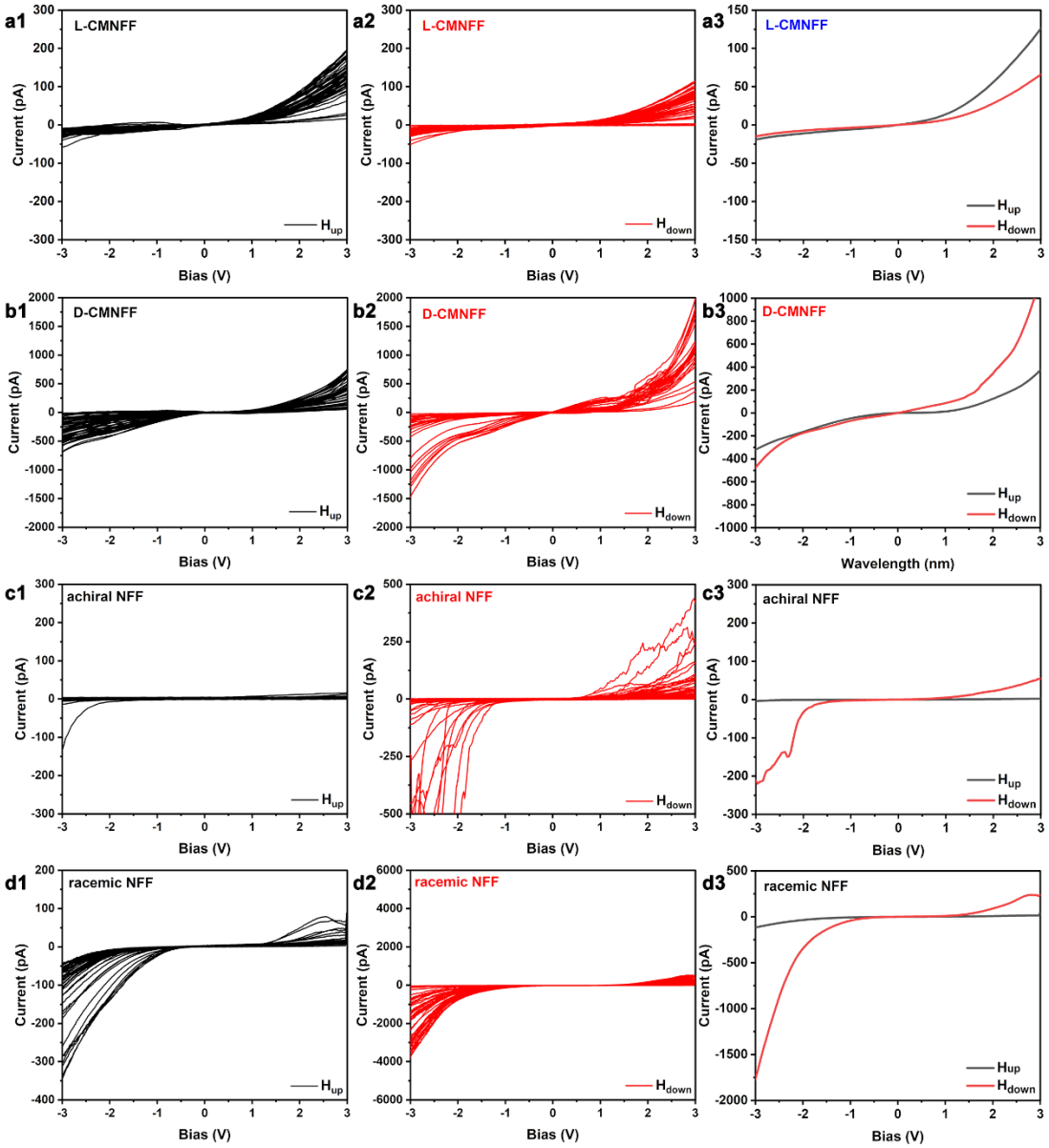

Figure S10. I-V curves obtained from antipodal CMNFFs, achiral NFF and racemic NFF.

As shown in **Figure S10**, the current as a function of the applied voltage I-V curves of L-CMNFF, D-CMNFF, achiral NFF and racemic NFF measured with the tips magnetized in the DOWN directions. (a3, b3, c3, d3) The averaged I-V data obtained from a1, b1, c1 , d1 and a2, b2, c2 , d2. Around 50 I-V curves were recorded and averaged for each magnetized orientation, each I-V curve was obtained over different points on the sample.

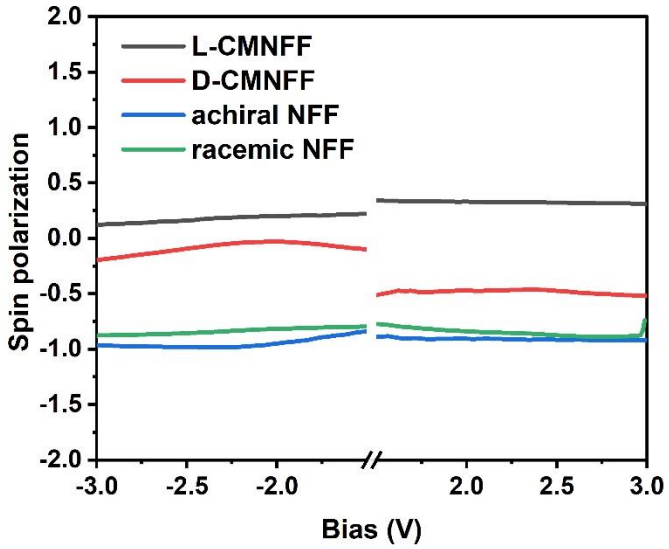

Figure S11. The spin polarization versus bias voltage curves of antipodal CMNFFs, achiral NFF and racemic NFFs.

As both the I_{UP} and I_{DOWN} in the bias voltage of -1.5 ~ 1.5 V were almost zero, the spin polarization was not inaccurate in the range of -1.5 ~ 1.5 V. The curves in this range were substituted with the symbol //.

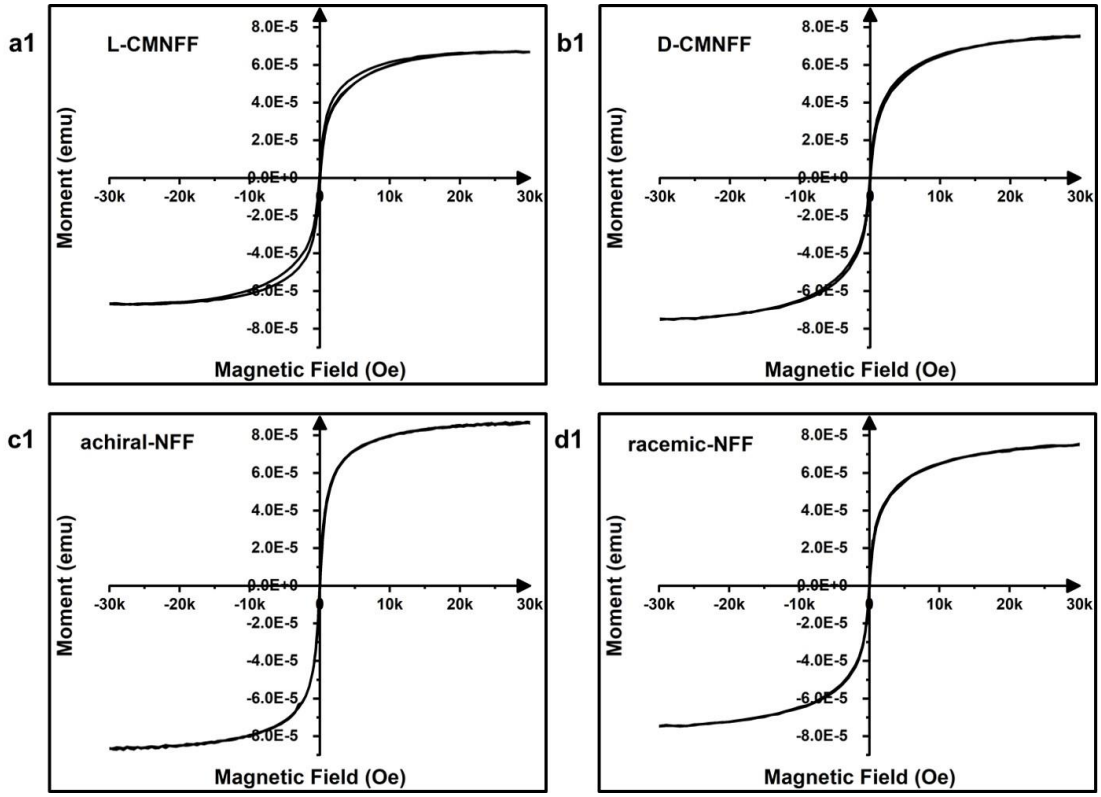

Figure S12. Magnetic hysteresis curves at room temperature of antipodal CMNFFs, achiral NFF, and racemic NFF.

All the samples show ferrimagnetic behaviour at room temperature.

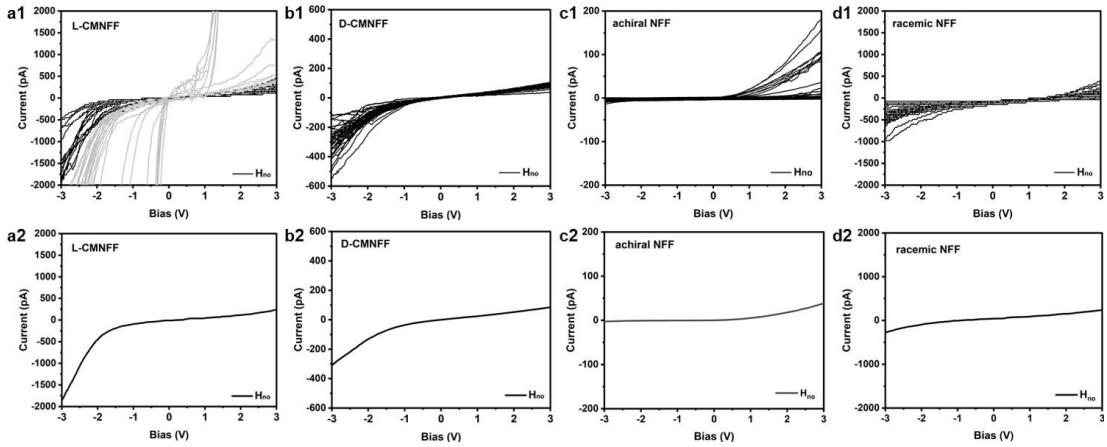

Figure S13. I-V curves obtained from L-CMNFF, D-CMNFF, achiral NFF and racemic NFF using conductance AFM with unmagnetized tips.

The conductance AFM with unmagnetized tips of L-CMNFF, D-CMNFF, achiral NFF and racemic NFF have been measured (**Figure S13**). Some I-V curves of L-CMNFF are out of range due to the destruction of films by the current (gray lines in **Figure S13a1**), which are not used for accumulation. Similar but relatively weak current can be observed from these samples. It indicates that the current arises from the tunnel magnetoresistance (TMR) of a magnetic tunnel junction (MTJ). That is, the current observed in the mc-AFM measurements depend on whether the excited electrons in our films and the tip are predominantly spin-up or spin-down (which can be called spin polarization), rather than on the magnetic moment orientation or magnetism. Besides, it indicates that the influence from magnetic field of magnetized tip is so small that can be negligible.

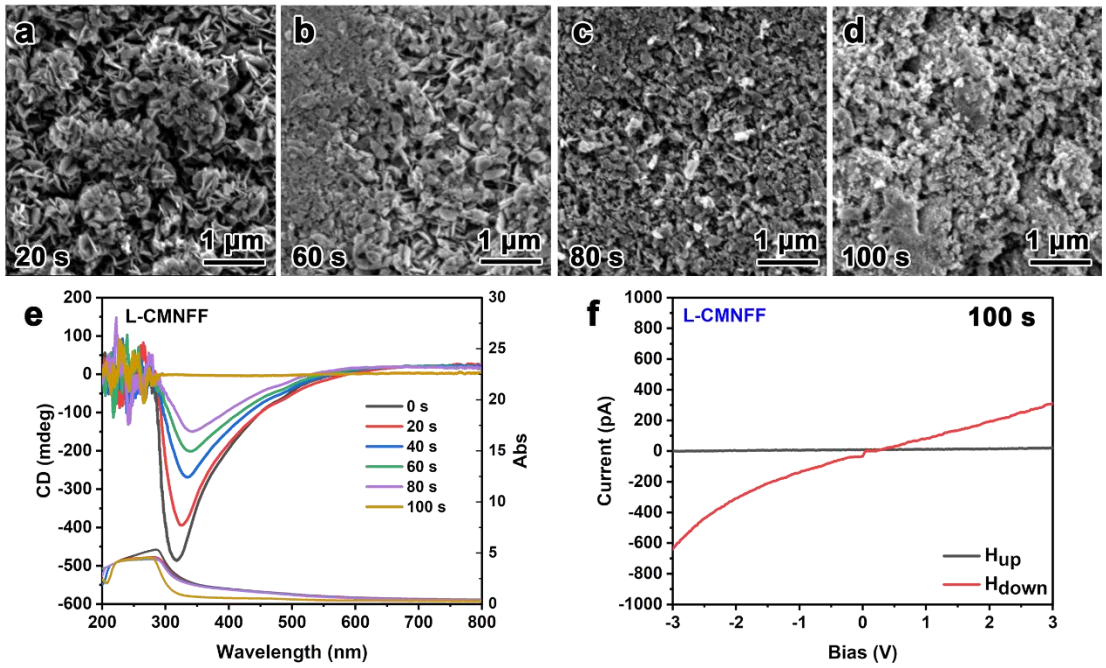

Figure S14. (a-d) SEM images, and (e) corresponding transmitted CD (top lines) and UV-visible (bottom lines) spectra with different peening time. (f) The mc AFM- measurement on L-CMNFF with peening 100 s.

A L-CMNFF were shattered by peening with different time. As shown in **Figure S14**, the

hierarchically chiral structures were collapsed into aggregates and finally destroyed with increasing peening time. Meanwhile, the CD signals of these samples were significantly decreased upon destruction of chiral mesostructures. The current of destroyed L-CMNFF increased more with DOWN direction magnetized tip than that with UP direction magnetized tip, which is opposite to the original L-CMNFF but agree with the achiral NFF. It is deduced that the chirality induced spin selectivity disappeared with destroying chiral mesostructures, and the intrinsic spin polarization can be observed. The enhancement of current can be ascribed to the enhancement of charge carrier due to increasing defects.

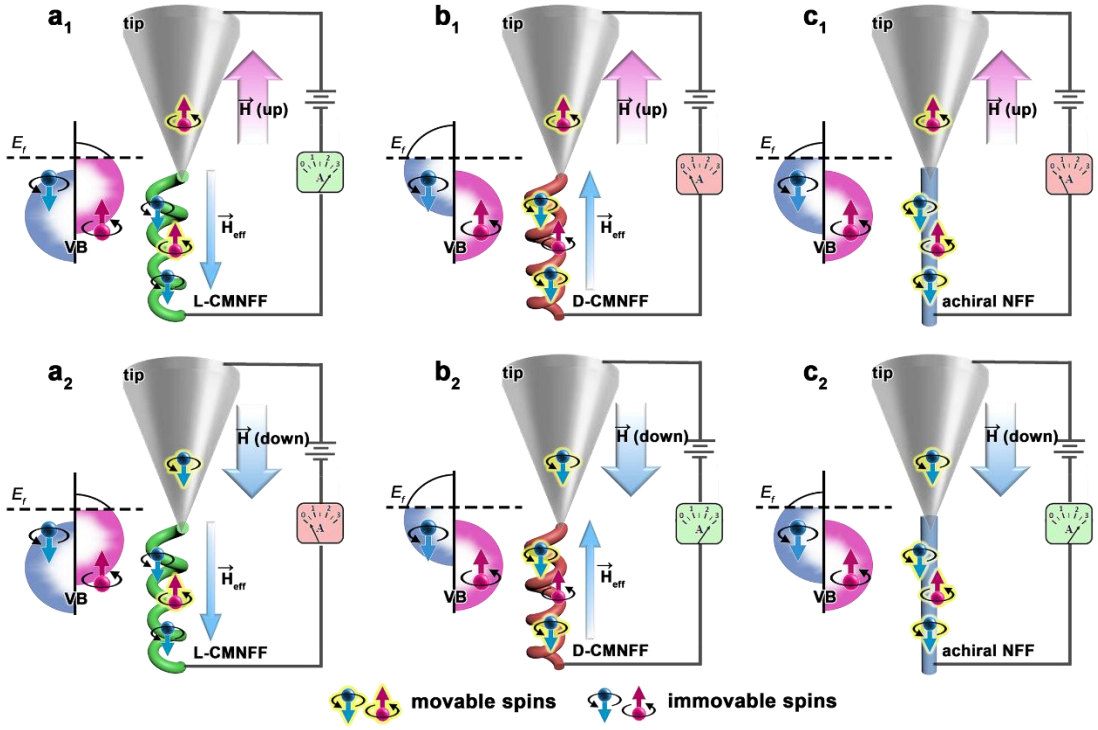

Figure S15. Schematic drawings of the parallel configuration with a high tunnelling current and antiparallel configuration with a low tunneling current between the tip and L-CMNFF (a), D-CMNFF (b), and achiral NFF (c).

In the achiral NFF (**Figure S15c**), intrinsic ferrimagnetism-induced spin polarization results that movable spins are dominantly parallel with the tip magnetized in the DOWN direction showing a high tunnelling current. In the L-CMNFF (**Figure S15a**), the competitive effect between intrinsic ferrimagnetism and chirality-induced spin selectivity and the latter is slightly stronger contribute to the result that movable spins are dominantly parallel with the tip magnetized in the UP direction, which show a slightly high tunnelling current. In the D-CMNFF (**Figure S15b**), the synergistic effect between intrinsic ferrimagnetism and chirality-induced spin selectivity results that movable spins are dominantly parallel with the tip magnetized in the DOWN direction showing a high tunnelling current.